Environment of Metal-O-Fe Bonds Enabling High Activity in CO_2 Reduction on Single Metal Atoms and on Supported Nanoparticles

Yifeng Zhu[†,§], Simuck F. Yuk[†], Jian Zheng[†], Manh-Thuong Nguyen[†], Mal-Soon Lee[†], Janos Szanyi[†], Libor Kovarik[†,‡], Zihua Zhu[‡], Mahalingam Balasubramanian[#], Vassiliki-Alexandra Glezakou[†], John L. Fulton[†], Johannes A. Lercher[†], Roger Rousseau*[,†], Oliver Y. Gutiérrez*[,†]

[†]Institute for Integrated Catalysis, Pacific Northwest National Laboratory, Richland, WA 99352, USA

[‡]William R. Wiley Environmental Molecular Sciences Laboratory, Pacific Northwest National Laboratory, Richland, WA 99352, USA

[#]Advanced Photon Source, Argonne National Laboratory, Argonne, IL 60439, USA

[§] Current address: Department of Chemistry, Fudan University, 200433, PRC

Supporting Information Placeholder

ABSTRACT: Single-atom catalysts are often reported to have catalytic properties that surpass those of nanoparticles, while a direct comparison of sites common and different for both is lacking. Here we show that single atoms of the Pt-group embedded into the surface of Fe_3O_4 have a greatly enhanced interaction strength with CO_2 compared with Fe_3O_4 surface. The strong CO_2 adsorption on single Rh atoms and corresponding low activation energies lead to two-orders-of-magnitude higher conversion rates of CO_2 compared to Rh nanoparticles. This high activity of single atoms stems from the partially oxidic state imposed by their coordination to the support. Fe_3O_4-supported Rh nanoparticles follow the behavior of single atoms for CO_2 interaction and reduction, which is attributed to the dominating role of partially oxidic sites at the Fe_3O_4-Rh interface. Thus, we show a likely common catalytic chemistry for two kinds of materials thought to be different, and we show that single atoms of Pt-group metals on Fe_3O_4 are an especially successful material for catalyzed reactions that depend primarily upon sites with the metal-O-Fe environment.

Introduction

Controlling the nuclearity of metal clusters and nanoparticles is a powerful strategy for tailoring their physicochemical properties and catalytic functionality.[1-4] However, it has been repeatedly stressed that activity versus size correlations do not hold as the size of metal particles approaches a few atoms.[5-6] The extreme case of single-metal atoms dispersed on oxidic supports frequently has been proposed to be superior in catalytic applications, outperforming traditional oxide-supported metal catalysts.[7-12]

However, the mechanisms that enable catalytic reactions with higher rates on single-atom catalysts than on traditional supported nanoparticles still are disputed. For example, a study concluded that single Ir atoms on $MgAl_2O_4$ coordinate with multiple ligands (CO and O species) to facilitate the oxidation of CO,[13] while single Pt atoms were found to increase the mobility of neighboring oxygen for CO oxidation, facilitating the addition of lattice oxygen to CO.[14-15] Several other studies have focused on underlining the chemical and catalytic differences between single-metal atoms and nanoparticles.[16-23] The interpretations of the results often are based on the premise that single-metal atoms and supported nanoparticles have intrinsically different properties. In contrast, we show here that single-metal atoms and supported nanoparticles share physicochemical properties resulting from the interface created by embedding the single atom and stabilizing the metal nanoparticle in the same environment.

We compare Rh single atoms stabilized on Fe_3O_4 with metal nanoparticles supported on Fe_3O_4 and SiO_2. The catalytic properties of the materials were studied for CO_2 reduction, which requires sites that polarize CO_2, while being able to generate and transfer hydrogen to the activated species.[24-26] The single Rh atoms interact more strongly with CO_2 than metallic Rh and selectively reduce CO_2 to CO with lower activation energy and with up to two-orders-of-magnitude higher rates. Interestingly, the catalytic properties of nanoparticles supported on Fe_3O_4 are more similar to the Rh single-atom catalysts than to nanoparticles supported on SiO_2.

Thus, the intermediate oxidation state (between metal and formal cation) that the support environment imposes (both interfaces and single atom sites) leads to more favorable interactions with adsorbing and reacting molecules. Namely, the ground state of adsorbed CO_2 is stabilized, while that of adsorbed CO is destabilized along the reaction pathways. The interplay between these changing competing states impacts the rates of the corresponding catalytic reactions. Detailed analyses of the physicochemical and catalytic properties of the single-metal sites and Fe_3O_4-supported nanoparticles confirmed the critical role of the metal-O-Fe environment on electronic properties of Pt-group metals and the resultant enhancements in the elementary steps of CO_2 reduction.

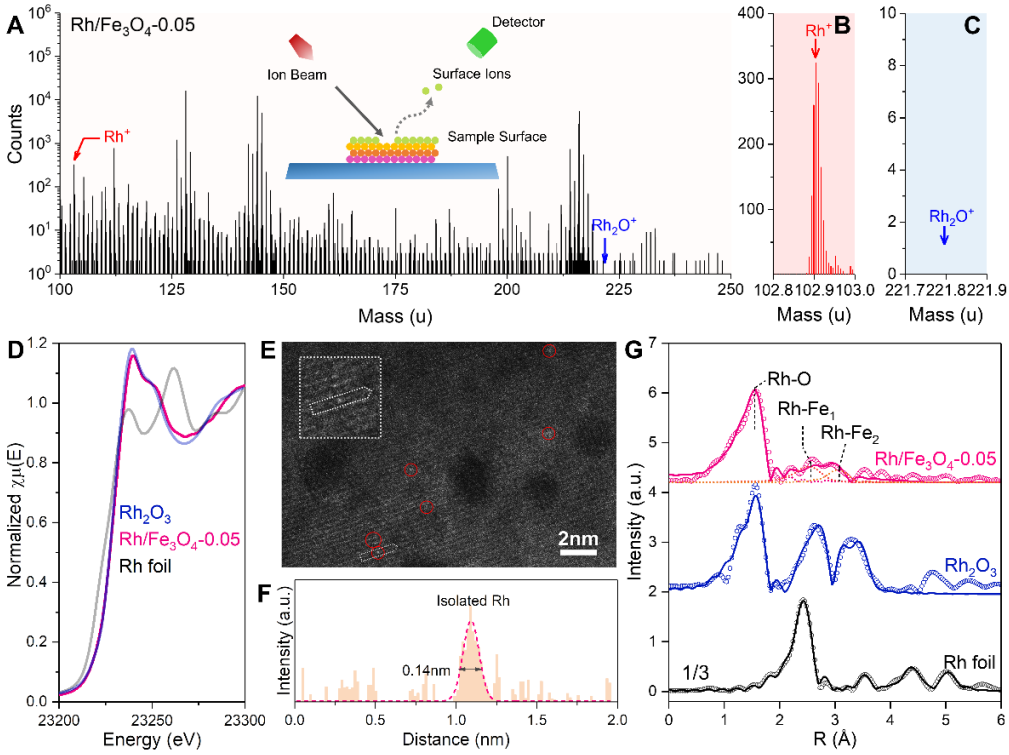

Figure 1. Characterization of isolated Rh atoms on magnetite (Rh/Fe_3O_4-0.05). (A, B, C) Time-of-flight secondary ion mass spectroscopy (TOF-SIMS) patterns show signals of Rh^+ fragments, whereas Rh_2O^+ fragments are absent, which indicates the presence of only isolated Rh atoms. (D) Rh K-edge X-ray absorption near edge structure (XANES) results of Rh/Fe_3O_4-0.05 and reference materials, which show that the environment of Rh in Rh/Fe_3O_4-0.05 is similar to the oxide reference in contrast to the metallic state of Rh in the foil. (E, F) High-angle annular dark-field scanning transmission electron microscopy (HAADF-STEM) results and the corresponding intensity profile in the direction marked by the arrow identifying the single atoms by its brightness (some are marked with red circles). (G) Experimental (dotted lines) and fitted (continuous lines) Rh K-edge extended X-ray absorption fine structure (EXAFS), which shows that Rh in Rh/Fe_3O_4-0.05 is coordinated with O atoms in the first shell (Rh-O) and surrounded by Fe atoms in the second ($Rh\text{-}Fe_1$) and third ($Rh\text{-}Fe_2$) shells contrasting the coordination of Rh in the reference Rh_2O_3 and Rh foil materials.

Results and Discussion

Single Rh atoms on Fe_3O_4

We prepared the Rh single-atom catalyst by depositing a small concentration of Rh cations on magnetite via a urea-hydrolysis method[27] (see supporting information for experimental details). The resulting material was denoted as Rh/Fe_3O_4-0.05, where 0.05 indicates 0.05 wt.% of Rh (**Table S1**). TOF-SIMS analysis identified the atomic dispersion of Rh at the Fe_3O_4 surface.[28-29] Rh_2O^+ species would have been detected by TOF-SIMS, if agglomerated RhO_x species were present. **Figures 1A–1C** notably show the absence of the Rh_2O^+ fragment, while the presence of monoatomic Rh^+ species is seen. This allows us to conclude that the concentration of metal particles, if any, in Rh/Fe_3O_4-0.05 is below the detection limit (5×10^6 to 5×10^8 atoms/cm^2, see experimental section for details).[30-31]

The intensity of the white line in the XANES results showed that the environment of Rh in Rh/Fe_3O_4-0.05 resembles that of the oxide reference and differs from the metallic state of Rh in the foil (**Figure 1D**). Independently, the isolated Rh atoms were imaged by HAADF-STEM as shown in **Figure 1E**. An exemplary line profile is shown in **Figure 1F**.

Rh K-edge EXAFS spectra of Rh/Fe_3O_4-0.05 are shown in **Figure 1G**. We attribute the feature at 2.02 Å to a Rh-O path with the coordination number (CN) of 5.5 (**Table S2**), indicating that the Rh atom is located at octahedral sites. A Rh-Rh path (expected at 2.66 Å) can be excluded from this fit. The second shell corresponds to a Rh-Fe path at 2.98 Å with a CN of 3.3. Conceptually, Rh should have six Fe neighbors, if it is in the bulk octahedral sites of Fe_3O_4. Thus, we conclude that isolated Rh atoms are anchored to undercoordinated octahedral positions at the surface. A direct bond between Rh and Fe in the form of Rh-Fe is excluded, because the Rh-Fe distance in the alloy is 2.53–2.59 Å (i.e., less than the distance of 2.98 Å that we observed).[32-34] The detailed description of the analysis of the X-ray spectra is provided in supplementary notes in **Tables S3–S6** and **Figures S1–S8** in the supporting information.

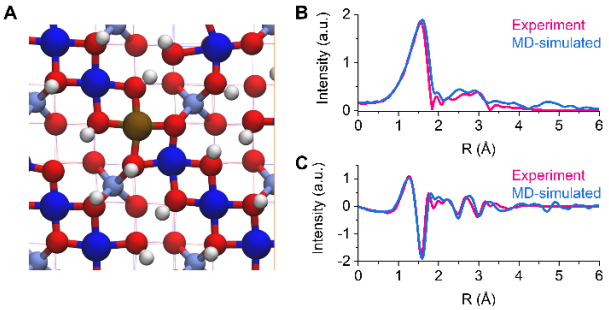

Figure 2. (A) Optimized geometry for single Rh atoms based on density functional theory (DFT) calculations in which a single Rh atom adopted the surface octahedral sites at 0.75 monolayer H coverage on $Fe_3O_4(001)$. Color codes: octahedral Fe (blue), tetrahedral Fe (light blue), Rh (brown), O (red), and H (white). Comparison of molecular dynamic (MD)-simulated EXAFS and experimental EXAFS spectra in magnitude part (B) and imaginary part (C) for Rh/Fe_3O_4-0.05. The MD-simulated EXAFS spectra were generated using the equilibrated MD trajectories at 300 K (please refer to the procedure associated with Figures S6–S7 for additional details).

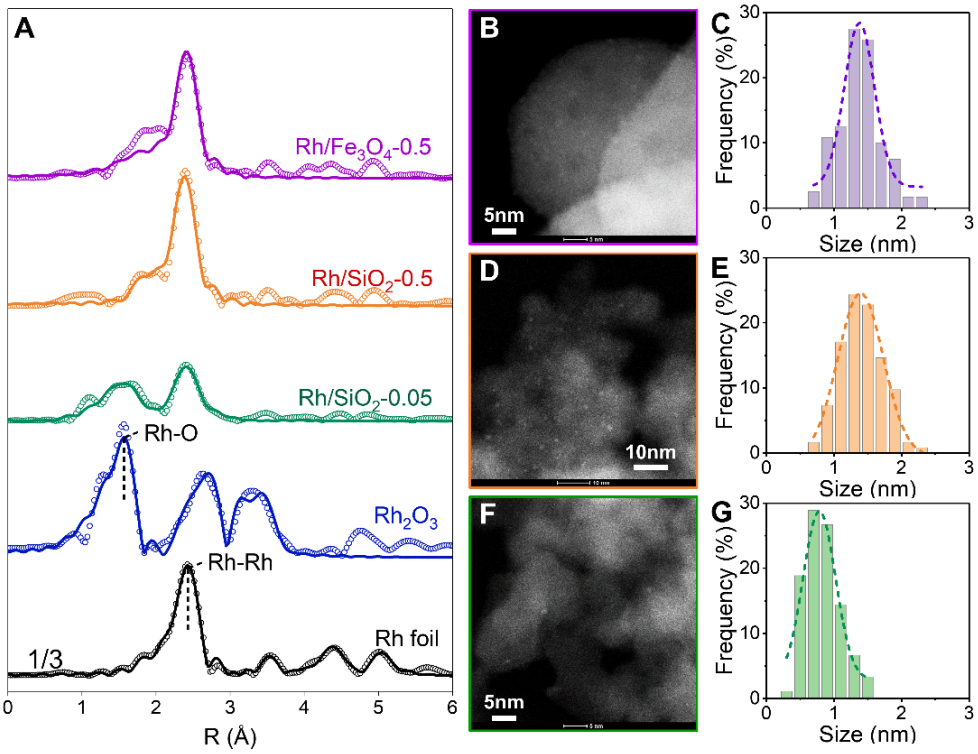

Figure 3. (A) Rh K-edge EXAFS spectra of selected catalysts. Representative HAADF-STEM images and particle size distribution histograms of Rh/Fe_3O_4-0.5 (B, C), Rh/SiO_2-0.5 (D, E) and Rh/SiO_2-0.05 (F, G). The points in Figure 3A are experimental data while the curves are the fitting results.

The concentration of surface hydroxyl groups (quantified by thermogravimetric and mass spectrometric analysis, **Figure S9**) formed during H_2 treatment and the reduction of CO_2 with H_2 was ~0.75 of a monolayer (OH/(Rh+Fe)). We used this information, the structure derived from EXAFS spectra, and the Fe_3O_4(001) model surface with subsurface cation vacancies proposed by Bliem et al.[35] to create a model for the single atom and its coordination environment by DFT calculations. We found excellent agreement between the experimental EXAFS spectra and those simulated for the model (**Figure 2A-2C**). In contrast to model Fe_3O_4 surfaces,[36-37] the high degree of hydroxylation of our material induces restructuring that eliminates subsurface cation vacancies. See the computational details and **Figure S4–S8** for a full discussion of the structural model and the EXAFS simulation.

Rh nanoparticles supported on Fe_3O_4 and SiO_2

At 0.5 wt.% Rh on Fe_3O_4 (labeled as Rh/Fe_3O_4-0.5), Rh nanoparticles formed (**Figure 3A–3C**). Rh_2O^+ fragments (and larger) were observed in TOF-SIMS results (**Figure S10**). The Rh nanoparticles observed by HAADF-STEM (**Figure 3B** and **S11**) had a narrow size distribution of 1–2 nm with a mean particle size of 1.4 nm and a dispersion of 78% (**Figure 3C**).

The EXAFS spectra of Rh/Fe_3O_4-0.5 showed a signal at 2.67 Å. We attribute this signal to a Rh-Rh path with a CN of 6.8 corresponding to an average number of 28–29 Rh atoms and a dispersion of 82 % (**Figures 3A** and **S12, Table S6**, see the supporting information for calculation details).[38-39] This is in agreement with results from the microscopy analysis. We attribute the signal at 2.02 Å to a Rh-O path with a CN of 0.7 that corresponds to Rh in the nanoparticle/Fe_3O_4 interface forming Rh-O-Fe bonds (**Table S6**). Such bonding requires that these Rh atoms have cationic character. This was confirmed by the intensity of the white line in the XANES results (**Figure S13**), which was higher for Rh/Fe_3O_4-0.5 than for the Rh foil (**Table S1**). In general, the oxidic nature of metal atoms at the interface of metal particles and oxide supports has been studied in a variety of cases by combining spectroscopy and theory. For example, there have been proposals of Ru clusters binding CeO_2 by Ru-O-Ce bonds.[40-41] Cu particles also bind via Cu-O-Zr bonds when supported on bulk ZrO_2 and on ZrO_2 clusters in metal organic frameworks.[26, 42] Pd clusters supported on FeO_x have higher oxidation state than metallic Pd.[43] In previous work, we found that an overlayer of FeO_x on Rh nanoparticles leads to the positively charged Rh species at the interfaces.[44]

To probe the potential impact of the interfacial Rh-O-Fe bond, varying concentrations of Rh were supported on SiO_2 (i.e., Rh/SiO_2-0.05 and Rh/SiO_2-0.5, the numbers indicate the wt.% loading). The TOF-SIMS spectra of these two materials showed large amounts of Rh_2O^+ fragments, expectedly suggesting that the average particle size increased with loading (**Figures S10**). The CN determined for the Rh-Rh path for Rh/SiO_2-0.05 was 4.2, corresponding to an average number of 8–9 Rh atoms constituting the particle and to a dispersion of 99% (**Figures 3A** and **S12**, **Table S7**). The Rh-Rh CN for Rh/SiO_2-0.5 was 6.7, indicating an average size of 28–29 Rh atoms and a dispersion of 83% (**Figures 3A** and **S12**, **Table S8**). This agrees well with the results of HAADF-STEM measurements (**Figures 3D** and **3E**) showing the average diameter of particles on Rh/SiO_2-0.5 to be 1.4 nm. For Rh/SiO_2-0.05, most of the Rh particles had a diameter below 1 nm, with an average diameter of 0.8 nm (**Figures 3F** and **3G**).

We analyzed further the Rh-O region (1–2 Å in R-space) of the XAFS spectra of Rh/Fe_3O_4-0.5, Rh/SiO_2-0.05, and Rh/SiO_2-0.5 (**Figure S14**). There is a Rh-O feature (evident when compared with the Rh_2O_3 reference) for Rh/SiO_2-0.5, but it is more evident for Rh/Fe_3O_4-0.5 and for Rh/SiO_2-0.05. This increasing contribution of the Rh-O path correlates well with the intensity of the white line of the XANES results (**Figure S13**). This correlation between XANES and XAFS results supports our interpretation that some Rh atoms had a cationic character due to the bond with oxygen for Rh/Fe_3O_4-0.5, Rh/SiO_2-0.05, and Rh/SiO_2-0.5.

Adsorption on single Rh atoms and Rh nanoparticles

The adsorption isotherms of CO_2, H_2, and CO on selected materials are shown in **Figure 4**. The catalysts containing Rh nanoparticles had maximum uptakes between 0.1 and 0.3 mol CO_2 per mol of exposed Rh. This agrees well with published results suggesting that CO_2 interacts weakly with metal surfaces.[45-46] In contrast, Rh/Fe_3O_4-0.05 showed a CO_2 uptake of 1.5 mol CO_2 per mol of Rh (**Figures 4A** and **4B**), while adsorption on bare Fe_3O_4 was only 20% of the total uptake observed for Rh/Fe_3O_4-0.05 (**Figures S15 and S16**).

Rh/Fe_3O_4-0.5 (Rh_{28} particles) showed a much lower CO_2 uptake than Rh/Fe_3O_4-0.05, despite both having nearly the identical fraction of Fe_3O_4 surface exposed (8.0 Fe/nm^2 for Rh/Fe_3O_4-0.5 and 8.4 Fe/nm^2 for Rh/Fe_3O_4-0.05). Thus, we conclude that Rh single atoms are part of the adsorption sites. In contrast to the strong interaction of single Rh atom sites with CO_2, the adsorption of CO and H_2 was low (**Figures 4C–4F**). The CO and H_2 uptakes on Rh/Fe_3O_4-0.05 were the lowest (<0.5 mol CO or H atoms per mole of isolated Rh at 33 kPa) followed by Rh/Fe_3O_4-0.5, and Rh supported on SiO_2.

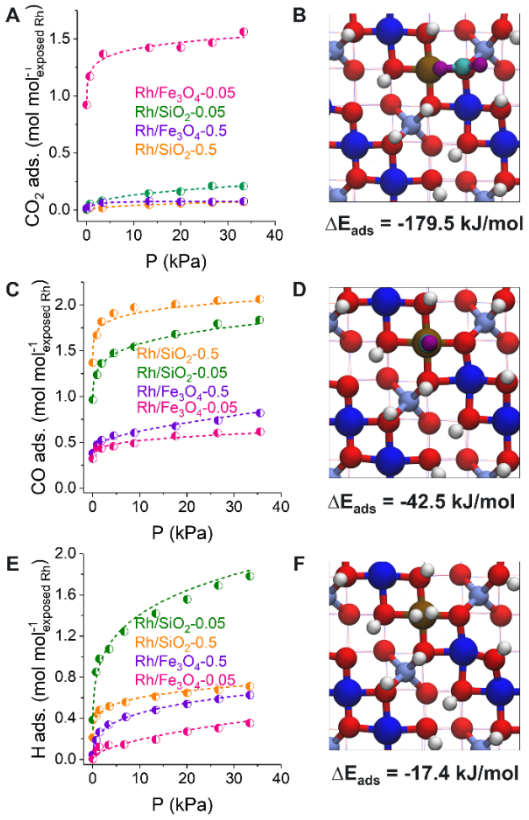

Figure 4. Adsorption isotherms, DFT-optimized geometry, and adsorption energy of CO_2 (A-B), CO (C-D) and H_2 (E-F) on single Rh atoms stabilized in Fe_3O_4 at 0.75 monolayer H coverage. A, C, and E also show the adsorption isotherms measured on Rh catalysts supported on Fe_3O_4 and SiO_2. The isotherms were taken at 308 K after treating the catalysts under H_2 flow in 473 K. The reference state of DFT-based adsorption energy is the bare Fe_3O_4(001) and gas-phase CO_2, CO, and H_2 molecules (see computational details for the definition of adsorption energy). Color codes: octahedral Fe (blue), tetrahedral Fe (light blue), Rh (brown), O (red), C (cyan), O of CO_2/CO (purple) and H (white).

Using a Langmuir formalism (i.e., constant heat of adsorption, reversibility of adsorption), we determined the adsorption equilibrium constants, which are compiled in **Table S9** (fitting lines are shown in **Figure 4**). The CO_2 adsorption equilibrium constant (K_{CO2}) for Rh/Fe_3O_4-0.05 (single Rh sites) was 551 (i.e., one to two orders of magnitude higher than for the catalysts with Rh nanoparticles). However, the adsorption equilibrium constant of CO (K_{CO}) for Rh/Fe_3O_4-0.05 was only 1.6 (i.e., one to two orders of magnitude lower than for catalysts containing Rh particles). We observed a similar, although less marked, trend for K_{ads} of H_2 (K_{H2}), which was 2 on Rh/Fe_3O_4-0.05 and 7–10 for Rh particles supported on Fe_3O_4 and SiO_2. We were able to measure the enthalpy of adsorption of CO_2 on Rh/Fe_3O_4-0.05 as ΔH = -93±6 kJ mol^{-1} and the enthalpy of adsorption as $T\Delta S$ = -93±6 kJ mol^{-1}. However, the uptakes of H_2 and CO were too low to be accurately measured.

DFT suggests that upon adsorption, CO_2 has one O atom directly bound to the Rh site, while the C atom binds to a neighboring surface O (**Figure 4B**), forming a carbonate. In qualitative agreement with the experiments, the resulting DFT adsorption energy of CO_2 was -180 kJ mol^{-1}. In contrast, the DFT adsorption energy of CO and H_2 were only -42 and -17 kJ mol^{-1}, respectively (**Figures 4D** and **4F**), indicating a much weaker adsorption.

The importance of the single Rh atom is seen when replacing the Rh atom with an Fe atom in the calculations, which decreased the interaction strength with CO_2 to 90 kJ mol^{-1}. Differences between Rh and Fe sites are attributed to their charge differences, with Rh being more reduced than Fe at the same location (**Figure S17A**). The base strength of oxide (favoring stabilization of carbonates) is enhanced with increasing surface coverages of H, as indicated by the slight increase in the negative Bader charge of surface O atoms (from -1.1 to -1.2 e$^-$). Thus, we conclude that higher coverages of hydroxyl groups promote the adsorption of CO_2 while suppressing the adsorption of CO (**Figure S17B**). Thus, the combination of both isolated Rh sites and the extent of hydroxylation influence the binding and reaction of CO_2.

Having established that single Rh atoms enhance the strength of interactions with CO_2, infrared (IR) spectroscopy was used to characterize the surface species. Upon contacting Rh/Fe_3O_4-0.05 with CO_2
(**Figures 5A and 5B**) at room temperature, bands assigned to hydroxy carbonate (1610, 1420, 1220 cm^{-1}), bidentate carbonate (1560, 1250 cm^{-1}) and ionic carbonate (1150 cm^{-1}) appeared, with the band intensities increasing with higher CO_2 pressure (see **Figure S18** for details of band assignments).[47-50] This confirmed that the carbonates are substantially better stabilized in the presence of single Rh atoms on Fe_3O_4. A band at 1350 cm^{-1} decreased upon CO_2 adsorption on Rh/Fe_3O_4-0.05 (**Figure 5A**); therefore, a negative signal is observed in the difference spectra (**Figure 5B**). We attribute such a band to the perturbation of hydroxyl groups associated with the adsorption of CO_2 and the concomitant formation of bicarbonates.[48-49] In contrast, after exposure of Rh/SiO_2-0.5 to CO_2 carbonate or bicarbonate species were not observed. Instead, linearly adsorbed CO was clearly visible, indicating a direct dissociation of CO_2 on metallic Rh (**Figure 5C**).[51-52]

Catalytic reduction of CO_2

The logarithmic dependence of the rates of reduction of CO_2 on the inverse temperature, selectivity, and related performance are depicted in **Figures 6 and S19–S23**. The apparent activation energy for CO_2 reduction on Rh/SiO_2 was 79-90 kJ mol^{-1} and decreased to 60 kJ mol^{-1} on Rh/Fe_3O_4-0.5 and 55 kJ mol^{-1} for Rh/Fe_3O_4-0.05 (**Figure 6**). CO and CH_4 were the only products under the reaction conditions used. Overall, the selectivity to CO increased with decreasing Rh particle size (**Figure S21**).

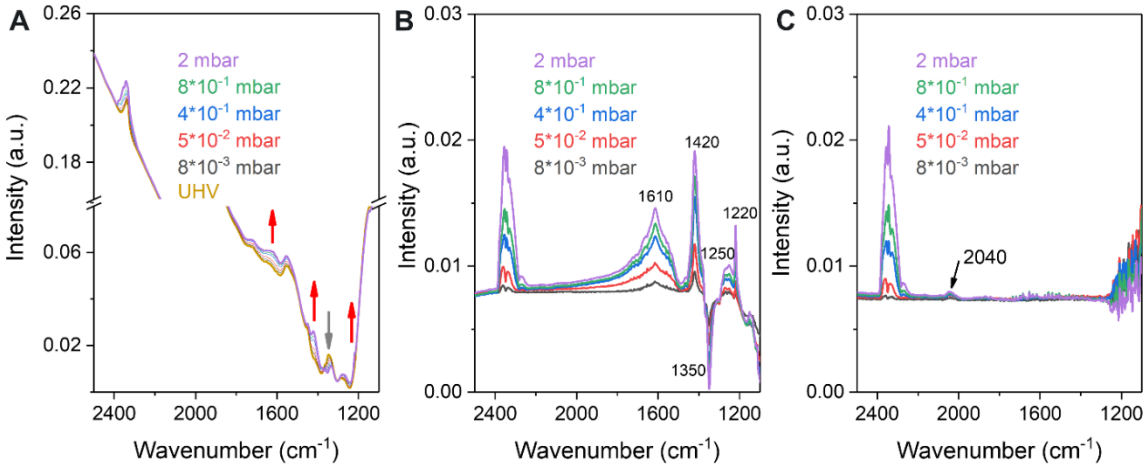

Figure 5. IR spectra of Rh/Fe_3O_4-0.05 exposed to CO_2 (A: original spectra; B: difference spectra) and difference IR spectra of Rh/SiO_2-0.5 (C) exposed to CO_2 at room temperature.

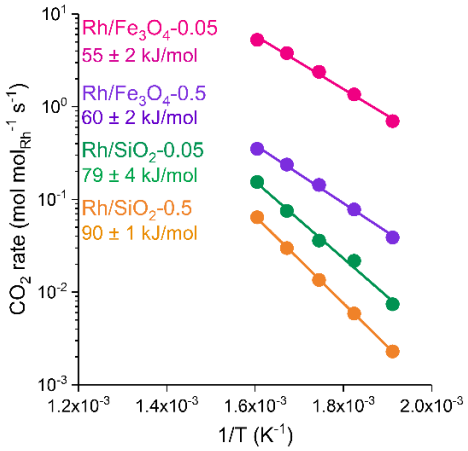

Figure 6. Catalytic performance of Rh catalysts in CO_2 reduction: Arrhenius plots for CO_2 conversion with rates normalized to the Rh content. Reaction conditions: 523–623 K, 101 kPa, $CO_2/H_2/He$ = 7/28/105 mL/min (gas hourly space velocity of 7×10^5 mL g^{-1} h^{-1}). Comparisons of rate normalized in other ways can be found in **Figures S19 and S20**.

For instance, the CO selectivity was approximately 30% on Rh/SiO_2-0.5 and increased to approximately 70 % on Rh/Fe_3O_4-0.5 and Rh/SiO_2-0.05. On Rh/Fe_3O_4-0.05, the CO selectivity was greater than 90%.

A two orders of magnitude higher CO_2 reduction rate (per Rh content) on Rh/Fe_3O_4-0.05 than on Rh/Fe_3O_4-0.5 highlights the importance of atomically dispersed Rh (**Figure S19**). On the other hand, Rh/Fe_3O_4-0.5 showed one to two orders of magnitude higher rates than Rh/SiO_2-0.5, pointing to the importance of Fe_3O_4 for the specificity of interaction of molecular species with the catalyst. Per exposed Rh, Rh/Fe_3O_4-0.05 leads to a rate as high as 5.3 s^{-1} at 623 K (i.e., two orders of magnitude higher than that of Rh/SiO_2-0.5) (**Figure 6**).

The rates normalized per exposed Rh, however, probably are not suitable for discussing the intrinsic activities of the catalysts because of the varying oxidation state of Rh (single metal atoms and metallic Rh nanoparticles). Thus, we compared the reaction rates normalized by the uptakes of CO_2 of the corresponding materials considering that such measurements serve as a titration of adsorption sites that can produce CO.[44] The comparison in **Figure S20** shows that the normalized rates of CO production on Rh/Fe_3O_4-0.05 and Rh/Fe_3O_4-0.5 are the same in most of the studied temperature ranges and higher than the rates observed on the SiO_2-supported catalysts. These observations allow us to propose that the highly active and selective sites in both the single Rh atoms and interfaces between Rh nanoparticles and Fe_3O_4 are similar. In view of the different activities observed over SiO_2-supported Rh and pure Fe_3O_4, we identify those possible sites as Rh-O-Fe bonds.

For Rh/Fe_3O_4-0.05 the reaction orders in CO_2 and H_2 were both 0.35, pointing to a relatively high CO_2 coverage and the lowest H_2 coverage among the studied catalysts. In contrast, the reaction order in H_2 was near zero, while the order in CO_2 order was 0.7 on Rh/SiO_2-0.5 (**Figure S21** and **Table S10**). This suggests a higher H_2 coverage and a lower CO_2 coverage on Rh nanoparticles. The H_2 order was 0.15 and the CO_2 order was 0.5 on Rh/Fe_3O_4-0.5, indicating that sites at the Rh-O-Fe perimeter contribute to changes in the coverage of adsorbed species (i.e., the abundance of H decreases, while that of CO_2 increases). The combination of higher rates with higher CO_2 surface coverage varying in parallel suggest that a higher number of possible transition states contributes to the higher rate as does the lower apparent activation energy (55 kJ mol^{-1} for single Rh sites compared to 90 kJ mol^{-1} on nanoparticles).

It has been concluded that the direct and reverse water-gas shift reactions on Fe_3O_4 occur through a redox or "regenerative" mechanism in which CO_2 as a reactant oxidizes a site on the surface. This site is reduced by H_2 removing oxygen in the form of water.[53-54] However, the large differences in activation energies that we observed on Fe_3O_4 and on Rh/Fe_3O_4-0.05 (129 kJ mol^{-1} and 55 kJ mol^{-1}, respectively) indicate that the incorporation of single Rh cations into the lattice shifts the reaction mechanism. The fractional reaction orders in CO_2 and H_2 (both around 0.35) observed on Rh/Fe_3O_4-0.05 further hint at an associative mechanism in which activated H interacts with adsorbed CO_2 to form an activated complex that ultimately decomposes to CO and H_2O. This surface complex usually is identified as a formate.[55-57] However, several dissenting studies have concluded that on some catalysts, formates are spectators, based on the mismatch between the kinetics of surface formates and the kinetics of products in the gas phase.[58] In these cases, instead of formates, carboxylates have been postulated as the associated complex that yields CO and hydroxyl groups (which desorb later as H_2O).[59-60] We resorted to DFT to explore the surface states over the optimized Rh-doped Fe_3O_4 surface comparing the energy level of adsorbed carboxylate (HOOC*) and a formate (HCOO*). We found a much lower stability for the latter (**Figure S23**) as some of us found in a previous work.[61] The formation of the possible formate intermediate is thermodynamically unfavorable compared even to the desorption of CO_2.

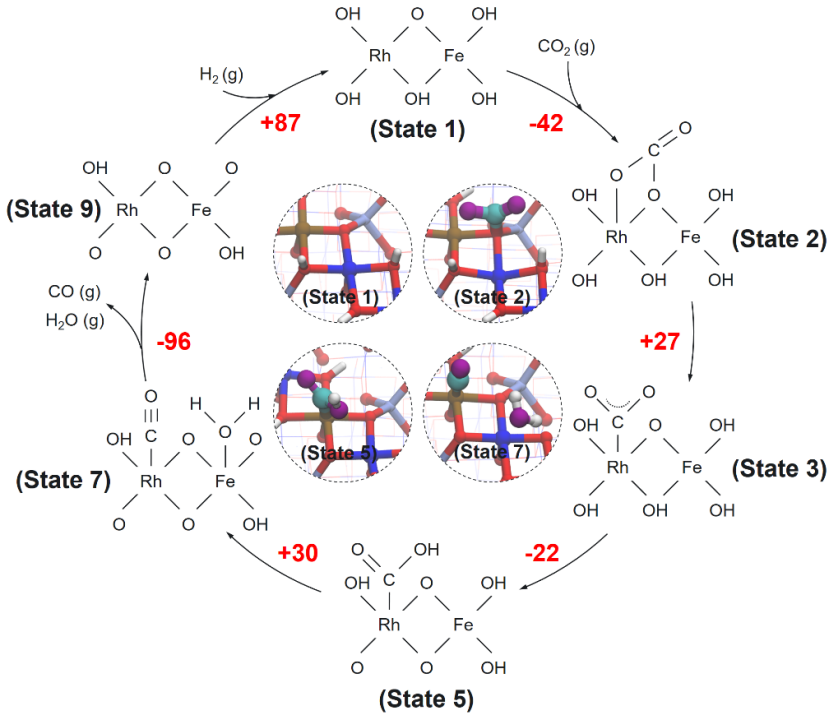

Figure 7. Proposed CO_2 reduction mechanism for reverse water-gas-shift over a single Rh atom embedded on a Fe_3O_4 surface at 0.75 monolayer H coverage. Red numbers represent standard Gibbs free difference ($\Delta G°$) between states in kJ mol^{-1}. More details can be found in **Figure S24**. The reference state of the DFT-based reaction pathway is the bare Fe_3O_4(001) and gas-phase CO_2 and H_2 molecules (see also computational details for the definition of adsorption energy).

Thus, we propose the mechanism shown in **Figure 7** and shown in detail in **Figure S24**. **State 1** is a site containing a single hydroxylated Rh atom, where CO_2 adsorbs. This yields a stable carbonate (or hydroxycarbonate) species depicted in **State 2** (also shown in **Figure 4B**). This surface species re-arranges to **State 3** which converts into the carboxylate intermediate upon reaction with surface OH groups and is shown in **State 5** in **Figure 7** (**State 4** and **State 6** are omitted for clarity but can be seen in **Figure S24** in the supporting information). The decomposition of the carboxylate into CO (located on the top of the Rh atom) and water (located on the top of an octahedral Fe atom) (**State 7**) is hypothesized to include the rate determining step. This agrees with the positive standard Gibbs free change calculated by DFT and with the negligible kinetic isotope effect measured by switching from H_2 to D_2 (**Figure S22**) (i.e., the rate-determining step does not involve hydrogen addition). The next steps in the catalytic cycle involve the desorption of CO and the elimination of H_2O, which results in the formation of the stable Rh/Fe_3O_4 surface (**State 9** in **Figure 7**). Subsequently, H_2 adsorbs on top of the atom, thereby regenerating the surface OH groups via dissociation steps and H diffusion. All intermediate steps (e.g., **State 4** and **State 6** and **State 8**) are shown in **Figure S24B**.

In **State 5** (**Figure 7**), the bond between the site containing Rh and the carboxylate, HOOC-Rh, is enabled by the electron-rich state of Rh produced by the adsorption of H_2. Bader charge analysis confirms the formal oxidation state of single Rh atom to be ~2 at 0.75 monolayer H coverage after calibrating Bader charges against known standards (**Table S11**). We conclude, thus, that the presence of more reduced Rh cations in the active site and the shift of the mechanism from a redox-type reaction on Fe_3O_4 (which requires switching between Fe^{3+} and Fe^{4+}) to a low-temperature associative mechanism is responsible for the very low activation barrier on the single-atom catalyst. We note in passing that upon heterolytic H_2 dissociation, an intermediate surface H with a hydride nature on the Rh site will likely transfer as a proton to yield a hydroxyl group reducing the metal center in the process.[62]

In **State 7** (**Figure 7**), the weak binding strength of the single atom for CO enables facile CO desorption and concomitantly high CO selectivity. On Rh nanoparticles, the stronger interaction of CO formed leads to a larger surface concentration and increases the possibility of C-O bond cleavage followed by complete hydrogenation to CH_4. The interaction of H_2 with the metal sites, on the other hand, is not a key feature for the observed rates, as H_2 activation and addition is not the part of the rate-determining step.

Characterization of spent catalysts

We did not find agglomerated Rh atoms, by HAADF-STEM in the Rh/Fe_3O_4-0.05 catalyst exposed to the reaction mixture (CO_2 and H_2) at 523 K. In agreement, the XANES and EXAFS results indicate that Rh remains isolated and Rh-Rh bonds are not observed (**Figure S25**). The white line of the XANES of the spent catalyst is less intense than that of the fresh Rh/Fe_3O_4-0.05 and a shoulder appears at 1.9 Å in the EXAFS. We attribute these variations to molecular species binding to the Rh sites, because changes in the Rh-Rh and Rh-O CNs were not found. This conclusion is line with the Bader charge analysis and calculations in **Figure S17**.

The HAADF-STEM characterization of the spent Rh/Fe_3O_4-0.5 and the corresponding statistical analysis did not show any appreciable change in the particle size distribution nor the presence of single atoms (**Figure S26**). The XANES spectra (**Figure S27**) did not show any appreciable difference compared to the fresh catalyst (i.e., both are close to the spectrum of the Rh foil).

Comparison of Rh/Fe_3O_4, Pt/Fe_3O_4, and Ru/Fe_3O_4 single-atom catalysts

To explore whether the described behavior of Rh is a singularity, we also prepared Fe_3O_4-supported Pt and Ru catalysts with similar low loadings (i.e., Pt/Fe_3O_4-0.05 and Ru/Fe_3O_4-0.05). To assure atomic dispersion, these catalysts were characterized by EXAFS (see the results for Ru/Fe_3O_4-0.05 in **Figure S28** and Pt/Fe_3O_4-0.05

in **Figure S29**). These two materials showed also remarkably high CO_2 uptakes (**Figure S16**) and negligible CO and H_2 uptakes during chemisorption experiments. The similarities among all the tested single atoms catalysts indicate that the strong adsorption of CO_2 on single metal sites stabilized by Fe_3O_4 is a general and indispensable property. The catalytic consequences of the similarities were expectedly the high selectivity in the conversion of CO_2 to CO with high rates per exposed metal of 0.5 s^{-1}–0.9 s^{-1} and 5.3–9 s^{-1} (at 523 K and 623 K, respectively) and with activation energies similar to that observed on Rh/Fe_3O_4-0.05, i.e., 55-65 kJ mol^{-1} (entries 13–20 in **Table S12**). The differences among the catalytic performances of the investigated single-atom catalysts are minor, considering that Rh, Pt, and Ru have markedly different catalytic properties otherwise.[63-64] Interestingly, the activity trend observed for the series of single-atom catalysts investigated in this work (Ru/Fe_3O_4-0.05 < Rh/Fe_3O_4-0.05 < Pt/Fe_3O_4-0.05) coincides with the reactivity towards the decomposition of C1 oxygenated compounds on extended surfaces of the corresponding supported transition metals.[65] This supports our hypothesis that decomposition of surface carboxylates is the rate determining step and that this is common for all catalysts we investigated. We speculate that the relatively minor activity differences we observed are related to the semiconductor nature of the support, which "buffers" the electronic differences of the cationic Rh, Pt, and Ru. Thus, electronic interactions between the single atom and the hosting oxide surface are more important than the nature of the single atom to determine the catalytic pathways and rates of CO_2 reduction.

Conclusions

The environment created by supporting single atoms of Pt-groups metals on Fe_3O_4 controls their interactions with CO_2 and CO. Specifically, strong interactions of CO_2 with single atoms are the key to a high concentration of transitions states and high rates of CO_2 reduction to CO. Shown in detail for Rh, the strong interactions are provided by the substitution of Fe^{3+}, at octahedral sites, by $Rh^{\delta+}$. These newly created single Rh atom sites, or more precisely Rh-O-Fe sites, stabilize surface carbonates upon CO_2 adsorption and offer a low energy pathway for the non-assisted decomposition of a carboxylate intermediate to CO and H_2O. The weak interaction of CO with the Rh-O-Fe site suppresses the hydrogenation of CO to methane under the explored reaction conditions. In stark contrast, weak interactions of Rh particles with CO_2 while strongly adsorbing CO, yield relatively low CO_2 conversion rates with high selectivity to CH_4.

The similar kinetic performance of Fe_3O_4-supported Rh particles and single Rh atoms for the production of CO allows us to hypothesize that the interfacial Rh-O-Fe bonds of Fe_3O_4-supported Rh nanoparticles have the same catalytic chemistry of single Rh sites. Moreover, the chemistry discovered for Rh-O-Fe is not a singularity of Rh but extends to Ru-O-Fe and Pt-O-Fe sites that show the same correlation between the strong interaction with CO_2 and the high activity for the reverse water-gas shift reaction. Thus, the effect that the environment (Fe_3O_4 in our study) induces on the electronic properties of Pt-group metal atoms is more important than the identity of such single atoms. However, single atom sites better utilize the doping transition metal and suppress methane production, which preferentially occurs at metal particles.

ASSOCIATED CONTENT

Supporting Information

The Supporting Information is available free of charge on the ACS Publications website. Experimental details, supplementary notes, Tables S1–S12, Figures S1–S29 can be found in the supporting information.

AUTHOR INFORMATION

Corresponding Authors

O. Gutiérrez: oliver.gutierrez@pnnl.gov
R. Rousseau: roger.rousseau@pnnl.gov

Notes

The authors declare no competing financial interests.

ACKNOWLEDGMENTS

This work is supported by the U.S. Department of Energy (DOE), Office of Science, Office of Basic Energy Sciences, Division of Chemical Sciences, Geosciences and Biosciences (Transdisciplinary Approaches to Realize Novel Catalytic Pathways to Energy Carriers, FWP 47319). Our research used resources of the Advanced Photon Source, a DOE-Office of Science user facility operated by Argonne National Laboratory, and was supported by DOE under Contract No. DE-AC02-06CH11357 and the Canadian Light Source and its funding partners. Portions of this work were performed at the William R. Wiley Environmental Molecular Sciences Laboratory (EMSL), a national scientific user facility sponsored by DOE's Office of Biological and Environmental Research and located at Pacific Northwest National Laboratory (PNNL). Computational resources were provided via user grants at EMSL, at PNNL's Research Computing facility, and at the National Energy Research Scientific Computing Center, a DOE Office of Science User Facility operated under Contract No. DE-AC02-05CH11231. PNNL is operated by Battelle for DOE under Contract DE-AC05-76RL01830.

REFERENCES

1. Cargnello, M.; Doan-Nguyen, V. V. T.; Gordon, T. R.; Diaz, R. E.; Stach, E. A.; Gorte, R. J.; Fornasiero, P.; Murray, C. B., Control of Metal Nanocrystal Size Reveals Metal-Support Interface Role for Ceria Catalysts. *Science* **2013,** *341* (6147), 771-773.
2. Farmer, J. A.; Campbell, C. T., Ceria Maintains Smaller Metal Catalyst Particles by Strong Metal-Support Bonding. *Science* **2010,** *329* (5994), 933-936.
3. Vogt, C.; Groeneveld, E.; Kamsma, G.; Nachtegaal, M.; Lu, L.; Kiely, C. J.; Berben, P. H.; Meirer, F.; Weckhuysen, B. M., Unravelling structure sensitivity in CO_2 hydrogenation over nickel. *Nat. Catal.* **2018,** *1* (2), 127-134.
4. Liu, L.; Corma, A., Metal Catalysts for Heterogeneous Catalysis: From Single Atoms to Nanoclusters and Nanoparticles. *Chem. Rev.* **2018,** *118* (10), 4981.
5. Campbell, C. T.; Mao, Z., Chemical Potential of Metal Atoms in Supported Nanoparticles: Dependence upon Particle Size and Support. *ACS Catal.* **2017,** *7* (12), 8460-8466.
6. Cui, X.; Li, W.; Ryabchuk, P.; Junge, K.; Beller, M., Bridging homogeneous and heterogeneous catalysis by heterogeneous single-metal-site catalysts. *Nat. Catal.* **2018,** *1* (6), 385.
7. Guo, X.; Fang, G.; Li, G.; Ma, H.; Fan, H.; Yu, L.; Ma, C.; Wu, X.; Deng, D.; Wei, M.; Tan, D.; Si, R.; Zhang, S.; Li, J.; Sun, L.; Tang, Z.; Pan, X.; Bao, X., Direct, Nonoxidative Conversion of Methane to Ethylene, Aromatics, and Hydrogen. *Science* **2014,** *344* (6184), 616-619.
8. Greiner, M. T.; Jones, T. E.; Beeg, S.; Zwiener, L.; Scherzer, M.; Girgsdies, F.; Piccinin, S.; Armbrüster, M.; Knop-Gericke, A.; Schlögl, R., Free-atom-like d states in single-atom alloy catalysts. *Nat. Chem.* **2018,** *10* (10), 1008-1015.
9. Liu, G.; Robertson, A. W.; Li, M. M.; Kuo, W. C. H.; Darby, M. T.; Muhieddine, M. H.; Lin, Y. C.; Suenaga, K.; Stamatakis, M.; Warner, J. H.; Tsang, S. C. E., MoS_2 monolayer catalyst doped with isolated Co atoms for the hydrodeoxygenation reaction. *Nat. Chem.* **2017,** *9* (8), 810-816.
10. Qiao, B.; Wang, A.; Yang, X.; Allard, L. F.; Jiang, Z.; Cui, Y.; Liu, J.; Li, J.; Zhang, T., Single-atom catalysis of CO oxidation using Pt_1/FeO_x. *Nat. Chem.* **2011,** *3* (8), 634-641.

11. Kyriakou, G.; Boucher, M. B.; Jewell, A. D.; Lewis, E. A.; Lawton, T. J.; Baber, A. E.; Tierney, H. L.; Flytzani-Stephanopoulos, M.; Sykes, E. C., Isolated metal atom geometries as a strategy for selective heterogeneous hydrogenations. *Science* **2012,** *335* (6073), 1209-12.
12. Yang, X.-F.; Wang, A.; Qiao, B.; Li, J.; Liu, J.; Zhang, T., Single-Atom Catalysts: A New Frontier in Heterogeneous Catalysis. *Acc. Chem. Res.* **2013,** *46* (8), 1740-1748.
13. Lu, Y.; Wang, J.; Yu, L.; Kovarik, L.; Zhang, X.; Hoffman, A. S.; Gallo, A.; Bare, S. R.; Sokaras, D.; Kroll, T.; Dagle, V.; Xin, H.; Karim, A. M., Identification of the active complex for CO oxidation over single-atom Ir-on-$MgAl_2O_4$ catalysts. *Nat. Catal.* **2019,** *2* (2), 149-156.
14. Nie, L.; Mei, D.; Xiong, H.; Peng, B.; Ren, Z.; Hernandez, X. I. P.; DeLaRiva, A.; Wang, M.; Engelhard, M. H.; Kovarik, L.; Datye, A. K.; Wang, Y., Activation of surface lattice oxygen in single-atom Pt/CeO_2 for low-temperature CO oxidation. *Science* **2017,** *358* (6369), 1419-1423.
15. Therrien, A. J.; Hensley, A. J. R.; Marcinkowski, M. D.; Zhang, R.; Lucci, F. R.; Coughlin, B.; Schilling, A. C.; McEwen, J.-S.; Sykes, E. C. H., An atomic-scale view of single-site Pt catalysis for low-temperature CO oxidation. *Nat. Catal.* **2018,** *1* (3), 192-198.
16. Ding, K.; Gulec, A.; Johnson, A. M.; Schweitzer, N. M.; Stucky, G. D.; Marks, L. D.; Stair, P. C., Identification of active sites in CO oxidation and water-gas shift over supported Pt catalysts. *Science* **2015,** *350* (6257), 189-192.
17. Matsubu, J. C.; Yang, V. N.; Christopher, P., Isolated metal active site concentration and stability control catalytic CO_2 reduction selectivity. *J. Am. Chem. Soc.* **2015,** *137* (8), 3076-84.
18. Guo, Y.; Mei, S.; Yuan, K.; Wang, D.-J.; Liu, H.-C.; Yan, C.-H.; Zhang, Y.-W., Low-Temperature CO_2 Methanation over CeO_2-Supported Ru Single Atoms, Nanoclusters, and Nanoparticles Competitively Tuned by Strong Metal–Support Interactions and H-Spillover Effect. *ACS Catal.* **2018**, 6203-6215.
19. Yang, M.; Li, S.; Wang, Y.; Herron, J. A.; Xu, Y.; Allard, L. F.; Lee, S.; Huang, J.; Mavrikakis, M.; Flytzani-Stephanopoulos, M., Catalytically active Au-$O(OH)_x$ species stabilized by alkali ions on zeolites and mesoporous oxides. *Science* **2014,** *346* (6216), 1498-1501.
20. Malta, G.; Kondrat, S. A.; Freakley, S. J.; Davies, C. J.; Lu, L.; Dawson, S.; Thetford, A.; Gibson, E. K.; Morgan, D. J.; Jones, W.; Wells, P. P.; Johnston, P.; Catlow, C. R. A.; Kiely, C. J.; Hutchings, G. J., Identification of single-site gold catalysis in acetylene hydrochlorination. *Science* **2017,** *355* (6332), 1399-1403.
21. Oliver-Meseguer, J.; Cabrero-Antonino, J. R.; Domínguez, I.; Leyva-Pérez, A.; Corma, A., Small Gold Clusters Formed in Solution Give Reaction Turnover Numbers of 10^7 at Room Temperature. *Science* **2012,** *338* (6113), 1452-1455.
22. Zhang, H.; Watanabe, T.; Okumura, M.; Haruta, M.; Toshima, N., Catalytically highly active top gold atom on palladium nanocluster. *Nat. Mater.* **2012,** *11* (1), 49.
23. Vile, G.; Albani, D.; Nachtegaal, M.; Chen, Z.; Dontsova, D.; Antonietti, M.; Lopez, N.; Perez-Ramirez, J., A stable single-site palladium catalyst for hydrogenations. *Angew. Chem. Int. Ed.* **2015,** *54* (38), 11265-9.
24. Kattel, S.; Liu, P.; Chen, J. G., Tuning Selectivity of CO_2 Hydrogenation Reactions at the Metal/Oxide Interface. *J. Am. Chem. Soc.* **2017,** *139* (29), 9739-9754.
25. Wang, X.; Shi, H.; Szanyi, J., Controlling selectivities in CO_2 reduction through mechanistic understanding. *Nat. Commun.* **2017,** *8* (1), 513.
26. Zhu, Y.; Zheng, J.; Ye, J.; Cui, Y.; Koh, K.; Kovarik, L.; Camaioni, D. M.; Fulton, J. L.; Truhlar, D. G.; Neurock, M.; Cramer, C. J.; Gutiérrez, O. Y.; Lercher, J. A., Copper-zirconia interfaces in UiO-66 enable selective catalytic hydrogenation of CO_2 to methanol. *Nature Commun.* **2020,** *11* (1), 5849.
27. Zhu, Y.; Kong, X.; Yin, J.; You, R.; Zhang, B.; Zheng, H.; Wen, X.; Zhu, Y.; Li, Y.-W., Covalent-bonding to irreducible SiO_2 leads to high-loading and atomically dispersed metal catalysts. *Journal of Catalysis* **2017,** *353*, 315-324.
28. Wang, Z.; Liu, B.; Zhao, E. W.; Jin, K.; Du, Y.; Neeway, J. J.; Ryan, J. V.; Hu, D.; Zhang, K. H. L.; Hong, M.; Le Guernic, S.; Thevuthasan, S.; Wang, F.; Zhu, Z., Argon Cluster Sputtering Source for ToF-SIMS Depth Profiling of Insulating Materials: High Sputter Rate and Accurate Interfacial Information. *J. Am. Soc. Mass Spectrom.* **2015,** *26* (8), 1283-1290.
29. Yan, F.; Liu, L.; Walsh, T. R.; Gong, Y.; El-Khoury, P. Z.; Zhang, Y.; Zhu, Z.; De Yoreo, J. J.; Engelhard, M. H.; Zhang, X.; Chen, C.-L., Controlled synthesis of highly-branched plasmonic gold nanoparticles through peptoid engineering. *Nat. Commun.* **2018,** *9* (1), 2327.
30. Douglas, M. A.; Chen, P. J., Quantitative trace metal analysis of silicon surfaces by ToF-SIMS. *Surface and Interface Analysis* **1998,** *26* (13), 984-994.
31. Ferlito, E. P.; Alnabulsi, S.; Mello, D., A different approach in sample preparation method for metallic contamination study by ToF-SIMS and TXRF. *Appl. Surf. Sci.* **2011,** *257* (23), 9925-9930.
32. Liao, F.; Lo, B. T.; Sexton, D.; Qu, J.; Ma, C.; Chan, R. C.-T.; Lu, Q.; Che, R.; Kwok, W.-M.; He, H.; Fairclough, S.; Tsang, S. C. E., A New Class of Tunable Heterojunction by using Two Support Materials for the Synthesis of Supported Bimetallic Catalysts. *ChemCatChem* **2015,** *7* (2), 230-235.
33. Palomino, R. M.; Magee, J. W.; Llorca, J.; Senanayake, S. D.; White, M. G., The effect of Fe–Rh alloying on CO hydrogenation to C_{2+} oxygenates. *J. Catal.* **2015,** *329*, 87-94.
34. Choong, C. K. S.; Chen, L.; Du, Y.; Schreyer, M.; Daniel Ong, S. W.; Poh, C. K.; Hong, L.; Borgna, A., The role of metal–support interaction for CO-free hydrogen from low temperature ethanol steam reforming on Rh–Fe catalysts. *Phys. Chem. Chem. Phys.* **2017,** *19* (6), 4199-4207.
35. Bliem, R.; McDermott, E.; Ferstl, P.; Setvin, M.; Gamba, O.; Pavelec, J.; Schneider, M. A.; Schmid, M.; Diebold, U.; Blaha, P.; Hammer, L.; Parkinson, G. S., Subsurface cation vacancy stabilization of the magnetite (001) surface. *Science* **2014,** *346* (6214), 1215-1218.
36. Parkinson, G. S.; Mulakaluri, N.; Losovyj, Y.; Jacobson, P.; Pentcheva, R.; Diebold, U., Semiconductor--half metal transition at the Fe_3O_4(001) surface upon hydrogen adsorption. *Phys. Rev. B* **2010,** *82* (12), 125413.
37. Doudin, N.; Yuk, S. F.; Marcinkowski, M. D.; Nguyen, M.-T.; Liu, J.-C.; Wang, Y.; Novotny, Z.; Kay, B. D.; Li, J.; Glezakou, V.-A.; Parkinson, G.; Rousseau, R.; Dohnálek, Z., Understanding Heterolytic H_2 Cleavage and Water-Assisted Hydrogen Spillover on Fe_3O_4(001)-Supported Single Palladium Atoms. *ACS Catal.* **2019,** *9* (9), 7876-7887.
38. Kip, B. J.; Duivenvoorden, F. B. M.; Koningsberger, D. C.; Prins, R., Determination of metal particle size of highly dispersed Rh, Ir, and Pt catalysts by hydrogen chemisorption and EXAFS. *J. Catal.* **1987,** *105* (1), 26-38.
39. Jentys, A., Estimation of mean size and shape of small metal particles by EXAFS. *Phys. Chem. Chem. Phys.* **1999,** *1* (17), 4059-4063.
40. Guo, Y.; Mei, S.; Yuan, K.; Wang, D.-J.; Liu, H.-C.; Yan, C.-H.; Zhang, Y.-W., Low-Temperature CO2 Methanation over CeO2-Supported Ru Single Atoms, Nanoclusters, and Nanoparticles Competitively Tuned by Strong Metal–Support Interactions and H-Spillover Effect. *ACS Catal.* **2018**, 6203-6215.
41. Wang, F.; Li, C.; Zhang, X.; Wei, M.; Evans, D. G.; Duan, X., Catalytic behavior of supported Ru nanoparticles on the {100}, {110}, and {111} facet of CeO2. *J. Catal.* **2015,** *329*, 177-186.
42. Larmier, K.; Liao, W. C.; Tada, S.; Lam, E.; Verel, R.; Bansode, A.; Urakawa, A.; Comas-Vives, A.; Coperet, C., CO_2-to-Methanol Hydrogenation on Zirconia-Supported Copper Nanoparticles: Reaction Intermediates and the Role of the Metal-Support Interface. *Angew. Chem. Int. Ed.* **2017,** *56* (9), 2318-2323.
43. Liu, J.; Wang, L.; Okejiri, F.; Luo, J.; Zhao, J.; Zhang, P.; Liu, M.; Yang, S.; Zhang, Z.; Song, W.; Zhu, W.; Liu, J.; Zhao, Z.; Feng, G.; Xu, C.; Dai, S., Deep Understanding of Strong Metal Interface Confinement: A Journey of Pd/FeOx Catalysts. *ACS Catal.* **2020,** *10* (15), 8950-8959.
44. Zhu, Y.; Zhang, X.; Koh, K.; Kovarik, L.; Fulton, J. L.; Rosso, K. M.; Gutierrez, O. Y., Inverse iron oxide/metal catalysts from galvanic replacement. *Nat. Commun.* **2020,** *11* (1), 3269.
45. Solymosi, F., The bonding, structure and reactions of CO_2 adsorbed on clean and promoted metal surfaces. *J. Mol. Catal.* **1991,** *65* (3), 337-358.
46. Solymosi, F.; Bugyi, L., Adsorption and dissociation of CO_2 on a potassium-promoted Rh(111) surface. *J. Chem. Soc., Faraday Trans. 1: Phys. Chem. Conden. Phases* **1987,** *83* (7), 2015-2033.
47. Nagaoka, K.; Seshan, K.; Lercher, J. A.; Aika, K.-i., Activation mechanism of methane-derived coke (CH_x) by CO_2 during dry reforming of methane – comparison for Pt/Al_2O_3 and Pt/ZrO_2. *Catal. Lett.* **2000,** *70* (3), 109-116.

48. Busca, G.; Lorenzelli, V., Infrared spectroscopic identification of species arising from reactive adsorption of carbon oxides on metal oxide surfaces. *Mater. Chem.* **1982,** *7* (1), 89-126.
49. Collins, S. E.; Baltanás, M. A.; Bonivardi, A. L., An infrared study of the intermediates of methanol synthesis from carbon dioxide over Pd/β-Ga_2O_3. *J. Catal.* **2004,** *226* (2), 410-421.
50. Millet, M.-M.; Algara-Siller, G.; Wrabetz, S.; Mazheika, A.; Girgsdies, F.; Teschner, D.; Seitz, F.; Tarasov, A.; Levchenko, S. V.; Schlögl, R.; Frei, E., Ni Single Atom Catalysts for CO_2 Activation. *J. Am. Chem. Soc.* **2019,** *141* (6), 2451-2461.
51. Fisher, I. A.; Bell, A. T., A Comparative Study of CO and CO_2 Hydrogenation over Rh/SiO_2. *J. Catal.* **1996,** *162* (1), 54-65.
52. Wang, C.; Guan, E.; Wang, L.; Chu, X.; Wu, Z.; Zhang, J.; Yang, Z.; Jiang, Y.; Zhang, L.; Meng, X.; Gates, B. C.; Xiao, F.-S., Product Selectivity Controlled by Nanoporous Environments in Zeolite Crystals Enveloping Rhodium Nanoparticle Catalysts for CO_2 Hydrogenation. *J. Am. Chem. Soc.* **2019,** *141* (21), 8482-8488.
53. Rhodes, C.; Hutchings, G. J.; Ward, A. M., Water-gas shift reaction: finding the mechanistic boundary. *Catal. Today* **1995,** *23* (1), 43-58.
54. Spencer, M. S., On the activation energies of the forward and reverse water-gas shift reaction. *Catal. Lett.* **1995,** *32* (1), 9-13.
55. Wang, X.; Shi, H.; Kwak, J. H.; Szanyi, J., Mechanism of CO_2 Hydrogenation on Pd/Al_2O_3 Catalysts: Kinetics and Transient DRIFTS-MS Studies. *ACS Catal.* **2015,** *5* (11), 6337-6349.
56. Ratnasamy, C.; Wagner, J. P., Water Gas Shift Catalysis. *Catal. Rev.* **2009,** *51* (3), 325-440.
57. Senanayake, S. D.; Stacchiola, D.; Evans, J.; Estrella, M.; Barrio, L.; Pérez, M.; Hrbek, J.; Rodriguez, J. A., Probing the reaction intermediates for the water–gas shift over inverse CeO_x/Au(111) catalysts. *J. Catal.* **2010,** *271* (2), 392-400.
58. Meunier, F. C.; Goguet, A.; Hardacre, C.; Burch, R.; Thompsett, D., Quantitative DRIFTS investigation of possible reaction mechanisms for the water–gas shift reaction on high-activity Pt- and Au-based catalysts. *J. Catal.* **2007,** *252* (1), 18-22.
59. Gokhale, A. A.; Dumesic, J. A.; Mavrikakis, M., On the Mechanism of Low-Temperature Water Gas Shift Reaction on Copper. *J. Am. Chem. Soc.* **2008,** *130* (4), 1402-1414.
60. Fu, Q.; Saltsburg, H.; Flytzani-Stephanopoulos, M., Active Nonmetallic Au and Pt Species on Ceria-Based Water-Gas Shift Catalysts. *Science* **2003,** *301* (5635), 935-938.
61. Nelson, N. C.; Nguyen, M.-T.; Glezakou, V.-A.; Rousseau, R.; Szanyi, J., Carboxyl intermediate formation via an in situ-generated metastable active site during water-gas shift catalysis. *Nat. Catal.* **2019,** *2* (10), 916-924.
62. Yuk, S. F.; Collinge, G.; Nguyen, M.-T.; Lee, M.-S.; Glezakou, V.-A.; Rousseau, R., Selective acetylene hydrogenation over single metal atoms supported on Fe_3O_4(001): A first-principle study. *J. Chem. Phys.* **2020,** *152* (15), 154703.
63. Solymosi, F.; Erdöhelyi, A., Hydrogenation of CO_2 to CH_4 over alumina-supported noble metals. *Journal of Molecular Catalysis* **1980,** *8* (4), 471-474.
64. Panagiotopoulou, P., Hydrogenation of CO2 over supported noble metal catalysts. *Appl. Catal. A: Gen.* **2017,** *542*, 63-70.
65. Mavrikakis, M.; Barteau, M. A., Oxygenate reaction pathways on transition metal surfaces. *J. Mol. Catal. A: Chem.* **1998,** *131* (1), 135-147.